Ultrasonics 119 (2022) 106612

Contents lists available at ScienceDirect

Ultrasonics

journal homepage: www.elsevier.com/locate/ultras

Enhancing the spectral signatures of ultrasonic fluidic transducer pulses for improved time-of-flight measurements

Benjamin Bühling [a,*], Stefan Maack [a], Thorge Schweitzer [b], Christoph Strangfeld [a]

[a] Bundesanstalt für Materialforschung und -prüfung (BAM), Unter den Eichen 87, 12205, Berlin, Germany
[b] FDX Fluid Dynamix GmbH, Rohrdamm 88, 13629, Berlin, Germany

ARTICLE INFO

Keywords:
Air-coupled ultrasound
Fluidics
Signal processing
Pulse compression
MIMO
Hilbert transform

ABSTRACT

Air-coupled ultrasonic (ACU) testing has proven to be a valuable method for increasing the speed in non-destructive ultrasonic testing and the investigation of sensitive specimens. A major obstacle to implementing ACU methods is the significant signal power loss at the air–specimen and transducer–air interfaces. The loss between transducer and air can be eliminated by using recently developed fluidic transducers. These transducers use pressurized air and a natural flow instability to generate high sound power signals. Due to this self-excited flow instability, the individual pulses are dissimilar in length, amplitude, and phase. These amplitude and angle modulated pulses offer the great opportunity to further increase the signal-to-noise ratio with pulse compression methods.

In practice, multi-input multi-output (MIMO) setups reduce the time required to scan the specimen surface, but demand high pulse discriminability. By applying envelope removal techniques to the individual pulses, the pulse discriminability is increased allowing only the remaining phase information to be targeted for analysis. Finally, semi-synthetic experiments are presented to verify the applicability of the envelope removal method and highlight the suitability of the fluidic transducer for MIMO setups.

1. Introduction

Ultrasonic measurements are an essential tool in many fields of science, ranging from medical diagnostics [1] and autonomous vehicle positioning [2] to non-destructive testing (NDT) of materials. In NDT, ultrasonic testing (UT) is a common measurement technique used to obtain information about material parameters, structural information, or to detect flaws [3]. A large number of UT methods have been developed to this end, involving the measurement of ultrasonic properties such as amplitude [4–7], spectral information [8–11], attenuation [12–15] or time-of-flight (TOF) [13,16–18].

In TOF measurements, the time delay of a pulse passing through a specimen is used to obtain quantitative information about material properties such as thickness of the specimen or propagation velocity. While a number of techniques [19–21] have been developed for plate-like structures to simultaneously measure both thickness and velocity, in many cases prior knowledge about one is necessary to deduce the other from the measured TOF. Several factors affect the signal-to-noise ratio (SNR) of TOF measurements. Besides the absorption in the material, scattering and dispersion characteristics [22], the transducer coupling and the signal shape influence the SNR. Coupling directly affects the transmitted sound intensity, as a significant portion of the intensity generated by the transducer is reflected at the specimen surface. To minimize these losses, coupling agents are applied at the transducer–specimen interface. This preparation is time consuming and can damage the specimen. Immersing of the entire setup in a coupling agent, such as water [23], is used to speed up measurements since transducers can then be moved freely to any accessible surface of the specimen. However, this requires that the specimen be placed in a water tank and be robust enough not to be affected by the coupling agent. Such conditions do not exist when testing large civil structures [18], vehicles [24], or artworks [25]. Regarding time efficiency and feasibility of immersion, actuating directly into air, i.e. using air as a couplant, can be considered the optimal choice [26]. Conventional state-of-the-art air-coupled ultrasound (ACU) systems are based on capacitive and piezoelectric transducers [26]. However, the sound intensity transmission losses due to impedance mismatches at both the transducer–air and the air–specimen interfaces are enormous. For example, the two-way sound pressure insertion loss of a concrete specimen amounts to −75 dB [27]. The two-way transducer insertion loss, being −17.5 dB for a current experimental transducer [28] or −22.4 for a commercial one [29], is added to that.

* Corresponding author.
E-mail address: benjamin.buehling@bam.de (B. Bühling).

https://doi.org/10.1016/j.ultras.2021.106612
Received 9 July 2021; Received in revised form 15 September 2021; Accepted 8 October 2021
Available online 22 October 2021

A considerable variety of ultrasound generation approaches have been proposed to improve or replace capacitive and piezoelectric transducers. These include improved matching layers [30–32], alternative transducer materials [33–35], and the use of lasers [36,37], X-rays [38–40], microwaves [41,42] as well as thermo-acoustic [43–45] or plasma-acoustic transducers [46,47] for ultrasound generation. Recently, the fluidic transducer was presented [48,49], which is a completely new actuation method for ultrasound. The fluidic transducer, based on the operating principle of a fluidic switch [50,51], generates an acoustic signal in the low-frequency ultrasound range by rapidly switching pressurized air from one pressure outlet to another. Generating an ultrasonic signal using an air flow eliminates the impedance mismatch between the transducer and the air, offering the potential to achieve high pressure amplitudes.

A related approach of using continuous flow noise for non-contact materials testing was presented by McBride and Hutchison [52]. The signal generated with a fluidic transducer differs in that distinct pulses with dominant frequency components are generated instead of stationary flow noise. Another example of using gas jets in ACU was given by Choi et al. [53]. They showed that an acoustic signal can be focused if it propagates inside a jet that has a lower acoustic velocity than the surrounding air. Applied to the fluidic transducer, this approach is promising to focus every second pulse generated [48].

The fluidic transducer was originally designed for applications in NDT of civil structures. In this field, high sound pressures are required since a high penetration depth is needed for concrete inspection. Furthermore, transducers must be robust against dust, mechanical impacts and temperature variations, as the measurements are conducted *in-situ*. All these requirements are fulfilled by the fluidic transducer [48]. Moreover, the device is robust against electromagnetic fields and radiation, making it a suitable candidate for ultrasonic applications in further harsh environments.

The measurement speed, which is the most important parameter for efficient measurements when using ACU in NDT in civil engineering, can be further increased by using multi-input multi-output (MIMO) setups. For this, the signal waveforms need to be quasi-orthogonal so as not to interfere at the receiver and they should have a high SNR. However, the SNR of the fluidic transducer signal is in the range of 10 dB, which is comparatively low when the transducer is used in MIMO mode. Pulse compression (PuC) is a technique that provides both SNR enhancement and MIMO capabilities.

In first ultrasonic applications of PuC [54–56] in the 1970s, a random noise signal was used as the coded signal so that correlation of the input and output signals yielded a peak corresponding to the time delay. In the early 1980s, it was found that phase modulating a signal with pseudorandom binary codes, such as Golay codes or M-sequences [57–59], resulted in more predictable and reduced sidelobes of the correlation output, with the pulses being repeatable and quasi-orthogonal. Due to their advantages, binary phase modulation schemes have been successfully applied and further developed [60–63]. Other widely used modulation schemes in ultrasonic NDT are frequency modulated pulses, especially chirped pulses. Linearly increasing or decreasing frequency modulation functions are often used [64], both in contact [65,66] and air-coupled applications [23,67]. Although offering an easy envelope and bandwidth control as well as a sharp correlation peak [64], only two quasi-orthogonal signals can be created, limiting the applicability of linear chirps in MIMO setups [68]. Given the widespread availability of chirp generation hardware, Callegari et al. [68] recently proposed a random frequency modulation method requiring only minor changes in hardware configuration compared to a chirp setup. This method essentially refers back to the origins of pulse compression in ultrasonic testing by correlating a time-limited noise signal. Additionally, the generated noise-modulated pulses are quasi-orthogonal, enabling MIMO operation.

The research presented here aims to interpret the signal generated by a fluidic transducer as a randomly amplitude and frequency modulated signal and to exploit its intrinsic features for MIMO applications. In Section 2, the measurement setup is presented and the signal characteristics of the fluidic transducer are analyzed. Section 3, the fundamentals of signal modulation are briefly reviewed and the fluidic transducer signal is discussed in this framework. Based on this discussion, a signal processing approach is proposed that exploits the inherent random modulation properties of the fluidic transducer signal to increase the transducer's MIMO capabilities. In Section 4, the performance of the transducer in a realistic measurement setup is discussed, and a semi-synthetic experiment is performed to assess the MIMO capabilities of the transducer.

2. Setup, transducer and signal

2.1. Setup

A fluidic transducer is used for the experiments, which has the same internal geometry as the one used to quantify the acoustic field [48]. The transducer was developed by FDX Fluid Dynamix GmbH (Germany) and manufactured at the Federal Institute for Materials Research and Testing (BAM). To increase the signal amplitude, an exponential horn with a length of 86.6 mm and an exponent $\epsilon = 36.6$ [69] is mounted to its primary outlet (O1 in Fig. 2). The horn was additively manufactured using fused deposition modeling. The design goal of the horn was to improve impedance matching to increase the transducers directivity. The presented design has a cut-off frequency of 2 kHz. Furthermore, a silencer (AMTE brass silencer by Festo, Germany) is mounted at the secondary outlet (O2 in Fig. 2) to reduce flow noise when the transducer is in the *off* state. The control ports are operated using fast-switching solenoid valves (MHJ10 by Festo, Germany). The valves were triggered at a repetition rate of 5 Hz. A calibrated microphone and an accelerometer were used for the recordings. The frequency response of the preamplified 1/4″ microphone (MK301 and MV302 by Microtech Gefell GmbH, Germany) with a sensitivity of 5 mV/Pa is nearly linear up to 70 kHz and is calibrated up to 100 kHz. The uniaxial accelerometer (352M66 by PCB Piezotronics, USA) is operated with a signal conditioner (480B21 by PCB Piezotronics, USA) with a gain factor of 100 and has a frequency range of up to 60 kHz with a sensitivity of 11.5 mV/g. For both valve control and data acquisition, a multifunction I/O device (USB-6361 by National Instruments, USA) is used. In each setup, 100 pulses were recorded. The data were sampled at a rate of 500 kS/s.

The experimental investigation is carried out using two setups. Setup 1 (Fig. 1) is used to obtain the pulse characteristics of the fluidic transducer, as discussed in Section 2.3. The microphone is placed directly in the center of the horn mouth to capture the fluidic transducer signal without defocus effects and with minimal noise. Setup 2 (Fig. 1) is used to evaluate the MIMO capability of the fluidic transducer in a more realistic setup, discussed in Section 4. The transducer is directed at a 0.5 mm aluminum sheet. To set up a *semi-contact* sensor arrangement [70], an accelerometer is placed on the sheet's backside to receive the signal. The reference signal for correlation is acquired by the microphone, which is located off the acoustic axis to minimize the interference with the ultrasonic field. The microphone and aluminum sheet are placed at distances of 70 mm and 255 mm from the horn mouth.

In both setups, the acquired signals are bandpass filtered with frequency bounds of $(20, 100)$ kHz to capture all ultrasonic components that can be reliably measured with the microphone, as has been done previously [48].

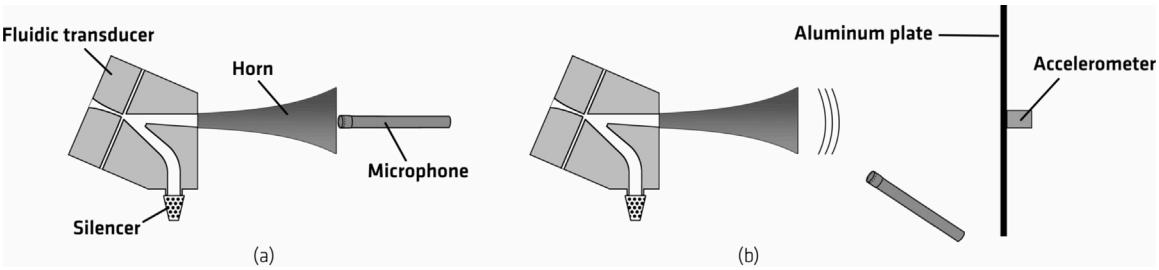

Fig. 1. Setup 1 with microphone directly in front of the horn (a) and setup 2 with microphone off the acoustic axis and accelerometer mounted on an aluminum plate (b).

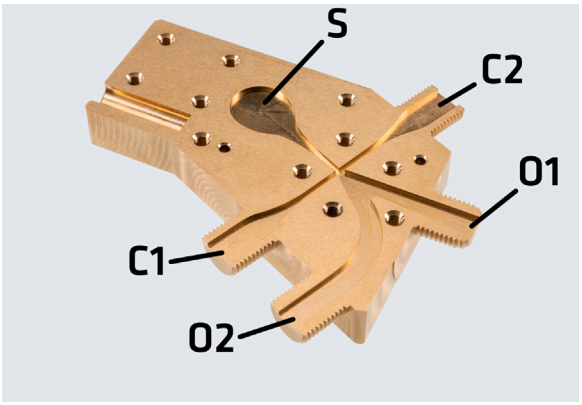

Fig. 2. Internal geometry of the fluidic transducer used in this study. S — supply port, C1 — control port 1 (switching *on*), C2 — control port 2 (switching *off*), O1 — outlet 1 (active during *on* state), O1 — outlet 2 (active during *off* state).

2.2. Fluidic transducer

The fluidic transducer (Fig. 2) generates an acoustic signal by causing rapid mass flow variations of pressurized air. Its geometry comprises a main air supply inlet, two control ports and two outlets. The supply air inlet operates with constant pressurized air, which leaves the device through one of the outlets. When an air mass flow is applied to one of the control ports, the main flow flips to the opposite outlet. The flow continues to exit through that outlet even when the control pressure is turned off. The fluidic transducer operates at two stable states, namely *on* and *off*, as well as in the switching of these two states. The acoustic signal is generated by these switching processes, in which the mass flow $\dot{m}$ strongly fluctuates when leaving the respective outlet. Subsequently, this causes pressure fluctuations $p(t,r)$ at a radial distance r as

$$p(t,r) = \frac{1}{4\pi r}\frac{d\dot{m}(t-\frac{r}{c})}{dt} \tag{1}$$

where c is the propagation velocity [71].

2.3. Signal

Fig. 3(a) shows a representative pulse in the time domain. The signal is similar to the previously published signal [48] because the internal geometry of the transducer has changed only slightly and the horn design dampens only frequencies <2 kHz. While the transducer is stably in *off* state, the recorded sound pressure consists of low-amplitude noise induced by the flow exiting through outlet 2. When the flow is switched to *on* state, an US peak is measured. The following higher amplitude noise is caused by the flow exiting through outlet 1 while the *on* state is stable. After switching *off* again, the flow returns to its initial state. Time frames are defined for the *on* and *off* states as well as for the switching process (Fig. 3(a)) The spectra in these time frames, averaged over all 100 switching processes recorded, are shown in Fig. 3(b). The generated pulse, covered by the switching time frame, contains dominant frequencies of around 30.4, 43.1, and 57.4 kHz. These three frequency peaks are distinct compared to the spectra of the *on* and *off* states. This frequency range allows detection of defects and material parameters at the scale of centimeters in typical construction materials like concrete or wood [72–74], for which the fluidic ultrasonic transducer has been developed.

Despite their average characteristic frequency peaks, the individual pulses generated by the fluidic transducer differ in onset, duration, and frequency content [48]. Thus, averaging to increase SNR is not feasible in TOF applications. Additionally, the high amplitude flow noise generated in the stable states limits the SNR of the pulse. The extraction of pulse features for TOF estimation, such as the onset or first maximum [12], is a challenging task under these high noise conditions. However, using a correlation approach alleviates the difficulties posed by the aforementioned behavior. Both onset jitter and duration can be compensated by defining a time window Δt in which the pulse is located. It also eliminates the need to pick out pulse features that may be hidden in the flow noise. The correlation approach is widely used in PuC methods and provides a framework useful for a deeper understanding of the fluidic transducer pulses and further utilization of its characteristic for MIMO applications. Accordingly, the random behavior of the pulses is interpreted as a non-deterministic amplitude and angle modulation of the transducer signal, using the framework provided by earlier studies on random modulation [54–56,68]. Demodulation techniques enable the extraction of unique pulse characteristics induced by the randomness of the modulation. The quasi-orthogonal pulses resulting from this signal processing then allow the use of fluidic transducers in MIMO applications.

3. Signal processing

Given the challenges posed by the previously discussed signal shape, further signal processing is required to improve TOF results in MIMO applications. After a brief revision of signal modulation principles and analytical signals, an envelope extraction method is presented that aims to reduce the mutual and self-interference of the signal.

3.1. Signal modulation

Commonly, an amplitude and angle modulated signal $s(t)$ is described as

$$s(t) = A(t)\cos(\omega_0 t + \phi_0 + \phi(t)) = A(t)g(t), \tag{2}$$

where $A(t)$ is the amplitude modulation (or signal envelope), ω_0 the carrier frequency, ϕ_0 the carrier phase shift, and $\phi(t)$ is the instantaneous phase inducing angle modulation [75]. In audiology, the term $g(t)$ containing the angle information is called temporal fine structure (TFS) [76]. Hereafter it will be termed unit envelope signal (UES) as it is the remainder when the envelope information $A(t)$ of the signal is removed. In frequency modulations, such as chirp methods, the angle modulation is given by the time derivative of instantaneous phase $\dot{\phi}(\tau)$, so that $\phi(t) = \int_0^t \dot{\phi}(\tau)d\tau$. Thus, angle modulation includes both phase

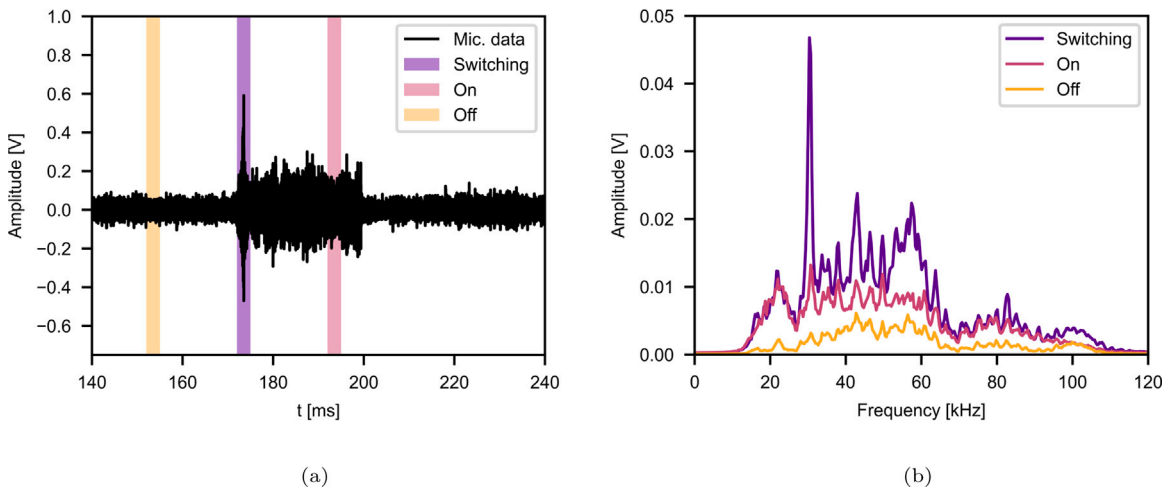

(a) (b)

Fig. 3. (a) Microphone time signal of one individual pulse in the time domain and (b) in the frequency domain, averaged over 100 pulses, in setup 1. The colored areas represent equal length time frames in the *on* and *off* states as well as during switching.

and frequency modulation, as one affects the other. In chirp modulations, the signal contains only one frequency component at any instant. For signals composed of multiple frequency components, the meaning of instantaneous frequency and phase is not trivial, as presented by Boashash [77]. One interpretation is that the instantaneous frequency represents the weighted average of all frequencies f_i that exist at a given time [78], so that

$$\frac{1}{2\pi}\frac{\Phi(t)}{dt} = \langle f_i \rangle_t. \tag{3}$$

This applies to both negative and positive frequencies, as the energy of a real signal is equally distributed in positive and negative frequencies. To find the TOF using a correlation approach, the received signal $s_r(t)$ is cross-correlated with the transmitted reference signal $s_t(t)$, so that

$$R_{tr} = s_r(t+\tau) * s_t(-t) \tag{4}$$

with

$$s_r(t) = s_t(t) * h(t) + n(t), \tag{5}$$

where $*$ denotes the convolution operator and R is the cross-correlation output. The filter function $h(t)$ contains any filtering along the signal path (e.g. by the specimen under test or varying frequency responses of transmitter and receiver) and $n(t)$ is the channel noise. Neglecting exterior influences and noise, Eq. (4) reduces to an autocorrelation $R_{tt} = R_{tr}$.

The Wiener–Khintchine theorem states that R_{tt} is the inverse Fourier transform of the power density spectrum of s_t [23]. Thus, the signal spectrum is shaped in PuC to enhance the correlation result further by reducing the sidelobe level of the autocorrelation function [23]. If the instantaneous phase or frequency *a priori* is known, such as in chirp applications, spectrum shaping can be accomplished by applying amplitude modulation to the signal. However, if this modulation is non-deterministic, the envelope of s_t depends fully on the transducer's impulse response to an *a priori* unknown excitation. The envelope can then have an adverse effect on the correlation output and diminish the quasi-orthogonality of angle-modulated signals needed to differentiate between various pulses in MIMO setups (Section 1). Even if the correlation output of the unit envelope signal components $g_r(t)$ and $g_t(t)$ is small, the correlation of the envelopes side may significantly enhance the correlation output of the signals in Eq. (4). Inserting Eq. (2) in Eq. (4), with an envelope function $A(t)$ that changes much slower than the respective $g(t)$, results in [79]:

$$R_{tr} = s_r * s_t = (A_r g_r) * (A_t g_t) = A_r A_t (g_r * g_t), \tag{6}$$

where the time arguments t and τ of the signal components are omitted for brevity. Thus, the product of $A_t A_r$ can mask a correlation output by creating secondary peaks where the phase-modulated signal is largely uncorrelated.

Fig. 4 shows an artificial example of envelope masking. A random bandpass signal g_r with an equally distributed spectrum in the $[40, 60]$ kHz interval is amplitude-modulated with a 25 Hz sinusoidal signal (Fig. 4(a)). When a partition of the unmodulated signal $g_r(\Delta t)$ is correlated with the whole signal g_r, a clear autocorrelation peak is found at a time shift of 0 ms (Fig. 4(b)). However, when the modulated signal is autocorrelated in the same way, the correlation peaks at time shifts with large envelope amplitude. Assuming that the TOF of a signal is indicated by the correlation maximum, the amplitude modulation would lead to a wrong TOF result.

Removing the envelope $A(t)$ from a signal, i.e. scaling it to unity, may thus enhance the discrimination of two pulses, which can be especially useful in random modulation applications. On the other hand, it may increase the overall noise floor, because the correlation output of low-amplitude noise is increased relative to high-amplitude pulse regions. Nevertheless, the pulses' unique spectral content and the relations between its components, i.e. the pulse's spectral signature, remains intact when removing the envelope information. The only linear operator that leaves the instantaneous phase and frequency unchanged when the signal power is scaled, e.g. by removing $A(t)$, is the Hilbert transform [80].

3.2. Hilbert transform

Following Ktonas and Papp [81], let $s(t)$ be in the form of Eq. (2). Since there is an infinite number of pairs of $(A(t), \phi(t))$ satisfying this decomposition, the concept of analytic signals is introduced. The analytic signal $z(t)$ associated with a real signal $s(t)$ contains only its positive frequency components and is therefore a complex signal of the form

$$z(t) = A(t)\exp(i\phi(t)). \tag{7}$$

Thus, a unique pair of $A(t) = |z(t)|$ and $\phi(t) = \arg(z(t))$ is obtained, while the original signal can be fully recovered as $s(t) = \mathrm{Re}(z(t))$. The Hilbert transform H is defined as

$$H(s(t)) = \frac{1}{\pi}\int_{-\infty}^{+\infty}\frac{s(\tau)}{t-\tau}\mathrm{d}t. \tag{8}$$

The Hilbert transform is the quadrature component of $s(t)$ and therefore eliminates all negative spectral components of $s(t)$ while doubling the positive ones. To construct an analytic function $z(t)$, the Hilbert transform $H(s(t))$ can be used [81], so that

$$z(t) = s(t) - iH(s(t)). \tag{9}$$

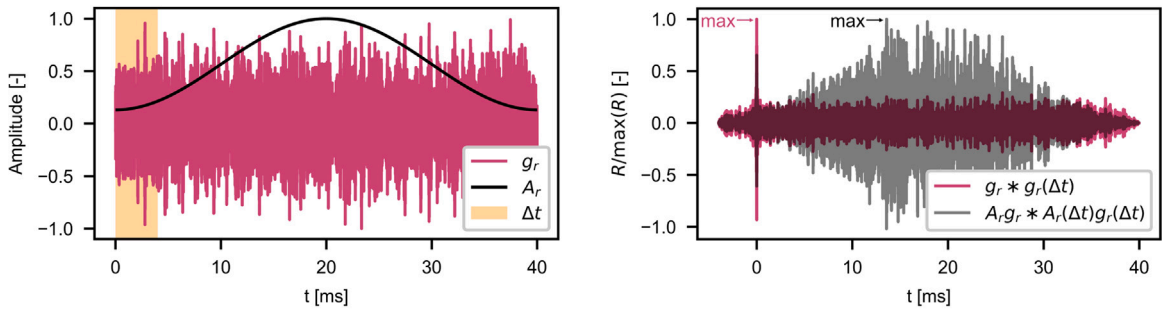

(a) (b)

Fig. 4. Artificial example of envelope masking using a random high frequency bandpass signal and a low frequency envelope (a) and the autocorrelation output of the modulated and unmodulated signals (b).

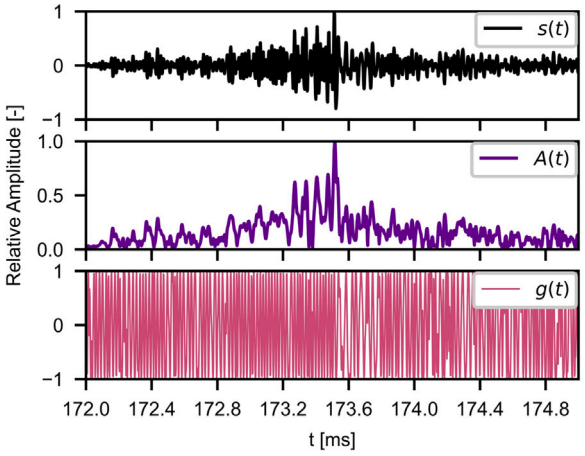

Fig. 5. The same signal as in Fig. 3 (top) with its decomposition in envelope $A(t)$(middle) and UES $g(t)$ (bottom).

This relation can then be used to remove the envelope information in Eq. (2) via Eq. (7), so that

$$g(t) = \cos(\arg(z(t))). \tag{10}$$

Fig. 5 shows the decomposition of the switching region of measured signal shown in Fig. 3(a) that is acquired by applying the Hilbert transform. While the signal envelope $A(t)$ exhibits high amplitudes in the peak region and lower amplitude in the *on* and *off* states, $g(t)$ is confined to the amplitude interval $[-1, 1]$ since it is defined as a cos function. Nevertheless, the angle variations manifest in the signal in $g(t)$ and an abrupt change in angle characteristic can even be observed visually around the peak region at $t = 173.6$ ms.

However, Eq. (9) holds only if the frequency bands of the envelope and phase functions are completely separated, as required by Bedrosian's product theorem [77]. If this condition is not met, a unique analytic signal $\hat{z}$ may still be found as

$$\hat{z}(t) = s(t) - iH(s(t)) = \hat{A}(t)\exp(\hat{\phi}(t)). \tag{11}$$

But $\hat{A}(t)$ and $\hat{\phi}(t)$ must not be considered independent, as it would be the case for band-separated $A(t)$ and $\phi(t)$. Instantaneous phase and envelope will overlap and be phase-distorted, and therefore lose their physical interpretability [77]. Since most measurement signals violate Bedosian's theorem, the concept of asymptotic analytic signals was introduced [82,83]: If the power of the overlapping frequencies become arbitrarily small, then $\hat{z}(t) \rightarrow z(t)$. This happens when the center frequency of a tight-band UES $g(t)$ is sufficiently far away from the band of lowpass signal envelope $A(t)$ such that, ideally, $\hat{\phi}(t) \rightarrow \infty$ [84]. In practice, however, Hilbert envelope extraction is used even when this condition is not met [83,85]. This results in mutual information being contained in $\hat{A}(t)$ and $\hat{\phi}(t)$ [86,87].

Thus, carrying out a Hilbert demodulation of a measurement signal to remove envelope masking can be considered a tradeoff between distortion and possibly improved MIMO capabilities. Hence, Hilbert demodulation is applied to all recorded fluidic transducer pulses. The spectral properties of the resulting signal envelope $\hat{A}(t)$ and the UES $\hat{g}(t)$ are evaluated to assess the applicability of Bedrosian's product theorem.

Fig. 6 shows the average power spectral density (PSD) of $s(t)$, $\hat{A}(t)$ and $\hat{g}(t)$ in the switching region shown in Fig. 3(a), scaled by the integral signal power. The signal has been lowpass filtered with a lower bound of 20 kHz before applying the envelope removal. The spectra of both $\hat{A}(t)$ and $\hat{g}(t)$ extend over the whole frequency range, thus violating Bedrosian's product theorem. Additionally, the plot shows the relative cumulative power of $\hat{A}(t)$ and $\hat{g}(t)$, with the sum starting at $f = 0$ Hz for the envelope and at the Nyquist frequency 250 kHz for the UES. If the bands were completely separated, the cumulative powers would have to touch in their separation interval, since their full cumulative power would be reached at the band limits. As a result, $A(t)$ and $g(t)$ would not be distorted. In the present case of overlapping bands, there is an intersection at a frequency of $f_c = 27.4$ kHz at a spectral power of 84%, meaning that this portion of the spectral powers at f_c is band separated. Comparing the PSDs of the original signal and the UES, both signals still show similar frequency peaks, while deviating slightly in amplitude over the whole frequency range. With a significant amount of power being band-separated and the frequency peaks of the spectra coincide, it is concluded that the pulse characteristics are preserved qualitatively when the signal envelope information is removed.

3.3. Mutual and self-interference

When correlation is applied for TOF estimation in MIMO setups, both mutual and self-interference of the pulses need to be considered. Mutual interference describes how similar the generated pulses are. If they are very similar, like the pulses produced by a capacitive transducer with no modulation, their cross-correlation is high and successive pulses are indistinguishable from each other. If the pulses have an ideally orthogonal basis, a nonzero correlation results only if the sent and received pulses are the same, i.e., the signal is autocorrelated. If the cross-correlation is very small compared to the autocorrelation of the pulse, successive pulses have little mutual interference and are considered quasi-orthogonal. Self-interference describes how clearly the TOF can be identified when the received pulse is correlated with the corresponding reference pulse. Small sidelobes indicate low self-interference as a high peak-to-sidelobe ratio reduces ambiguity concerning the correlation peak. The effects of Hilbert envelope extraction method on the mutual and self-interference of the fluidic transducer pulses are thus investigated.

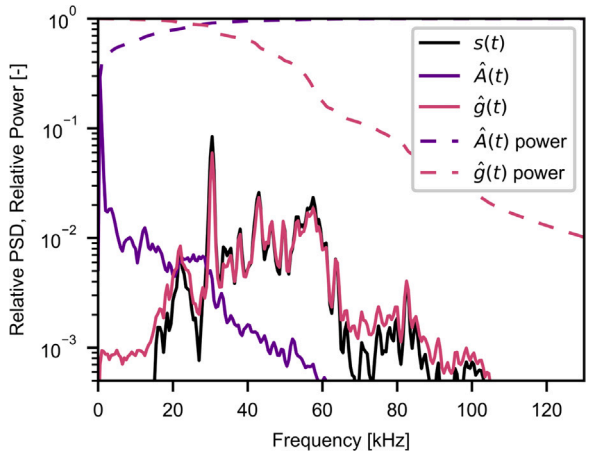

Fig. 6. Relative power spectral density and cumulative power averaged over all recorded pulses.

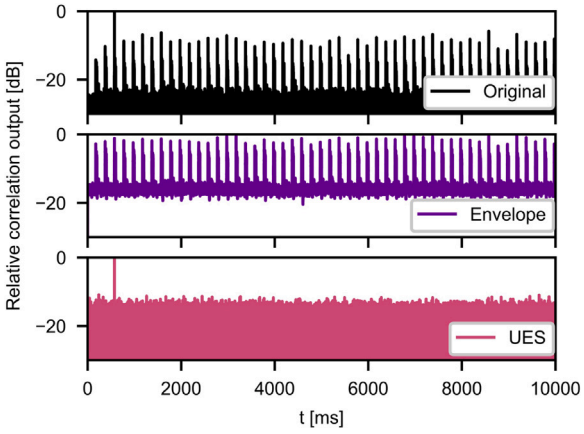

Fig. 7. Interference of one switching region, the third of the pulse train, with the first 50 switching cycles of the fluidic transducer in setup 1. The plots show the correlation of the original signal (top), the unit envelope signal (middle) and signal envelope (bottom).

Fig. 7 shows the correlation outputs of the original signal $s(t)$, the signal envelope $\hat{A}(t)$, and the UES $\hat{g}(t)$ when the switching region of a single pulse (which is the 3 ms region highlighted in Fig. 3(a) and shown in Fig. 5) is correlated with a pulse train containing 50 pulses. The original and envelope correlations show several correlation peaks at the time of switching. The multiple peaks in the original signal correlation output also indicate mutual information between the successive pulses. This is mainly contained in the signal envelope. While the UES correlation has only a noise floor everywhere except at the signal location, the envelope correlation has multiple peaks at all pulse locations. The envelope correlation even exhibits a maximum at the arrival time of a later pulse, highlighting the effect of envelope masking on mutual interference as given in Eq. (6).

To obtain more information on the mutual interference statistics of the signal components, all 100 recorded pulse switching time frames were individually correlated with the whole signal, as shown in Fig. 7. A histogram of the maximum mutual correlation amplitudes relative to their respective auto-correlations is shown in Fig. 8. The lower the relative correlation maxima, the higher is the orthogonality of the individual pulses. The original signal has a mean mutual interference of −8.9 dB with a standard deviation of 2 dB. The UES has a significantly lower mean of −11.9 dB with a standard deviation of only 0.6 dB. The envelope signal has the poorest performance with a mean of −1.6 dB and a standard deviation of 1.3 dB. Misidentification of a pulse or its

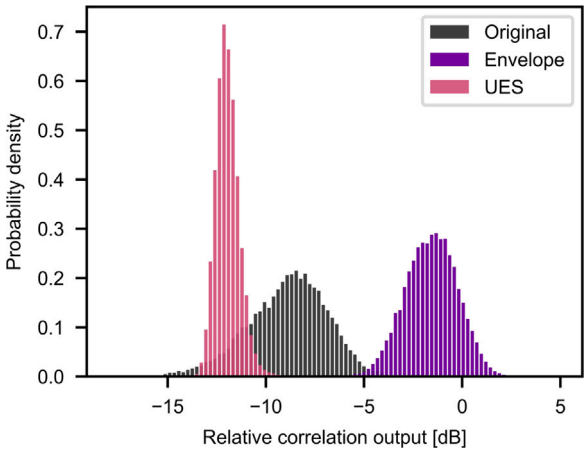

Fig. 8. Histogram of the maximum dB modulus of all mutual interferences calculated as shown in Fig. 7.

echoes in a MIMO setup is thus more likely if the original signal or its envelope is used for correlation rather than its UES.

The averaged correlation output of the peak region signal with the data of the whole switching cycle (Fig. 9(a)) highlights both adverse and beneficial effects of envelope masking on the self-interference in the original signal. While the switch is turned *off*, the signal received by the microphone has low amplitude, thus the average correlation modulus gives low values around −40 dB. It peaks at the pulse arrival time, as the correlation reduces to the autocorrelation close to $t = \tau$. While the transducer is in *on* state, the correlation modulus takes values < -30 dB since the average amplitude of the signal is higher than in the *off* state. When this amplitude information is removed by envelope extraction, the state of the fluidic transducer does not influence the correlation output, giving an average noise floor of around −30 dB. This output is higher than in the case of correlating the original signal, thus the inherent envelope masking improves the SNR at large time delays. Near the autocorrelation peak (Fig. 9(b)), envelope removal increases SNR, reducing sidelobe amplitude by 1.6 dB. The correlation sidelobe locations vary slightly between the original and demodulated signal due to the slight change in frequency content shown in Fig. 6.

4. Results and discussion of multisensor setup

The previous results have shown that interpreting the fluidic transducer signal as an amplitude and angle modulated signal and removing its envelope yields advantages, concerning both mutual and self-interference. To assess the effectivity of this approach in a more realistic setup, the same procedure was applied to the results obtained using measurement setup 2, which includes a thin aluminum plate as the specimen and an accelerometer as the receiving sensor. By using different sensors the performance of the envelope removal method is investigated, when sensor frequency responses and sensitivities differ. No measurable TOF change is induced by the aluminum sheet due to its thickness. A semi-synthetic experiment was then designed using the measured data to induce a variable artificial time lag and investigate the performance of the fluidic transducer in MIMO arrangements.

4.1. Pulse characteristics

Although the pulse is clearly distinguishable from the stable states of the fluidic switch, the SNR of the accelerometer signal is lower than that of the microphone signal (Fig. 10(a)). This is attributed to various factors that additionally influence the accelerometer signal: flexural waves and lamb waves of the aluminum plate as well as the lower sensitivity compared to the microphone. This behavior also becomes

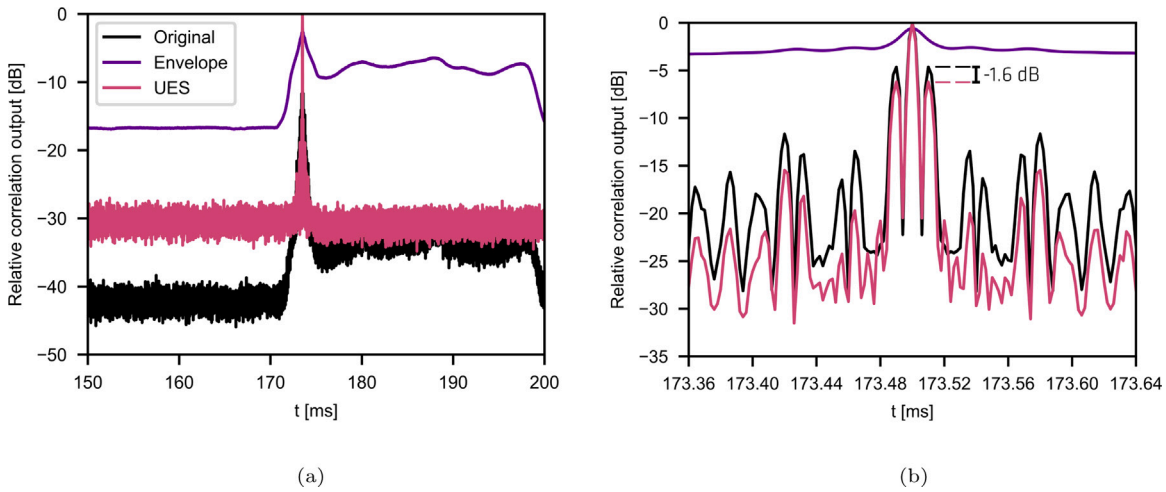

Fig. 9. Self-interference in setup 1 (a) through the part of the switching cycle and (b) zoom to the correlation peak area.

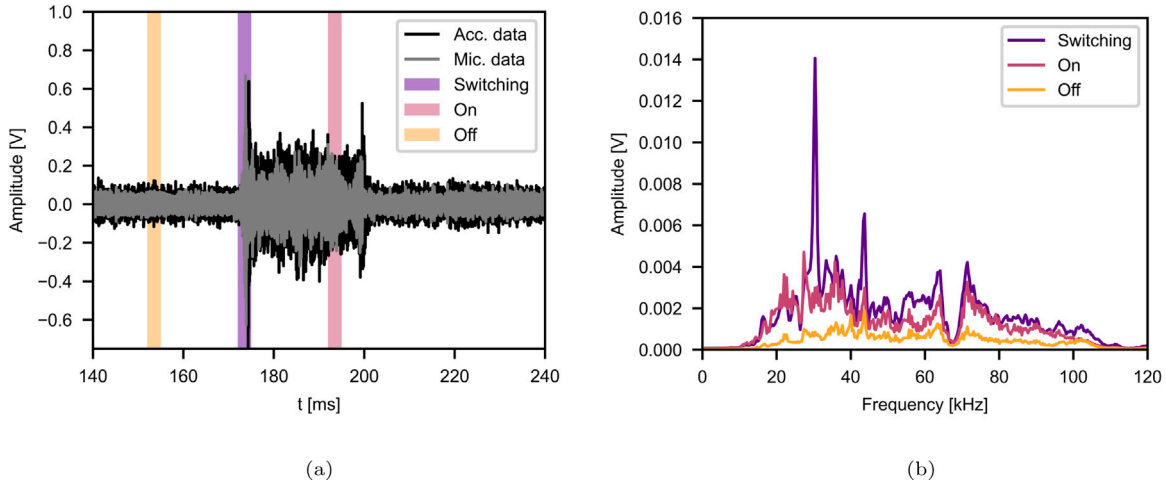

Fig. 10. (a) Microphone and accelerometer time signals of one individual pulse in time domain and (b) accelerometer signal in the frequency domain, averaged over 100 pulses, in setup 2. The colored areas represent equal length time frames in *on* and *off* states as well as during switching.

apparent when comparing the frequency domains of the accelerometer (Fig. 10(b)) and the microphone signal (Fig. 3(b)). While the frequency peaks are even more distinct in the switching region, their amplitude difference from the *on* and *off* states is reduced in the time signal. Furthermore, the main part of the additional noise is measured to occur at frequencies <40 kHz.

While the near sidelobes of the correlation result do not differ significantly between the original signals and the envelope-extracted signals, the far sidelobes are successfully attenuated by the reduced masking of the self-correlation result, as can be seen in Fig. 11(a). The overall peak-to-sidelobe ratio is significantly reduced compared to the pure microphone signal in Fig. 9(b). This is a result of the microphone signal being a sub-optimally matched filter to the accelerometer signal. The mutual interferences of all pulses are shown in Fig. 11(b). The results for the signal envelope are omitted as they were shown to give poor correlation results in Section 3.3. The average correlation modulus was reduced to −6.5 dB and −7.5 dB for the original signals and the UES, respectively. Their standard deviations are 2.3 dB and 0.9 dB, respectively. Thus, the mutual interference of the two signals in a realistic setup has been increased, while the difference in mean mutual interference has been decreased, i.e., the benefit of envelope removal has been reduced. This is attributed to receiver channel noise and varying sensor cut-off frequencies, which reduce the contribution of the spectral signature to the correlation output. Nonetheless, even when using sensors with different frequency responses the source pulse could be distinguished more clearly from other pulses by using the UES than by using the original signal for correlation.

4.2. Semi-synthetic experiment

In a MIMO setup, every receiver records a signal $\tilde{s_r}(t)$, which is a sum of multiple transmitter signals $s_{r,j}(t)$. The signals contained in $\tilde{s_r}$ did not necessarily arrive at the same point in time as different material properties in their propagation paths, sensor locations, or jitter in the pulsing may resulted in different TOFs. These same parameters may also result in attenuation of $s_{r,i}$. For the experiment $n = (2, 4)$, the signals recorded in setup 2 were scaled and time-shifted to generate these synthetic mixed signals so that

$$\tilde{s_r}(t, \alpha, \tau) = s_{r,0}(t) + \alpha \sum_{j=1}^{n} s_{r,j}(t + j\tau), \tag{12}$$

where α is a scaling factor modeling attenuation, and τ is the time shift of the added signals. Fig. 12 shows the construction of a signal according to Eq. (12). In Fig. 12, two signals are added, where the second is scaled by $\alpha = 0.4$. The resulting combined signal shows a large resemblance to the unattenuated signal component. In Fig. 12(b), three signals are added, which are time-shifted from their preceding signal by $\tau = 0.2$ ms. The combined signal shows that time shift makes

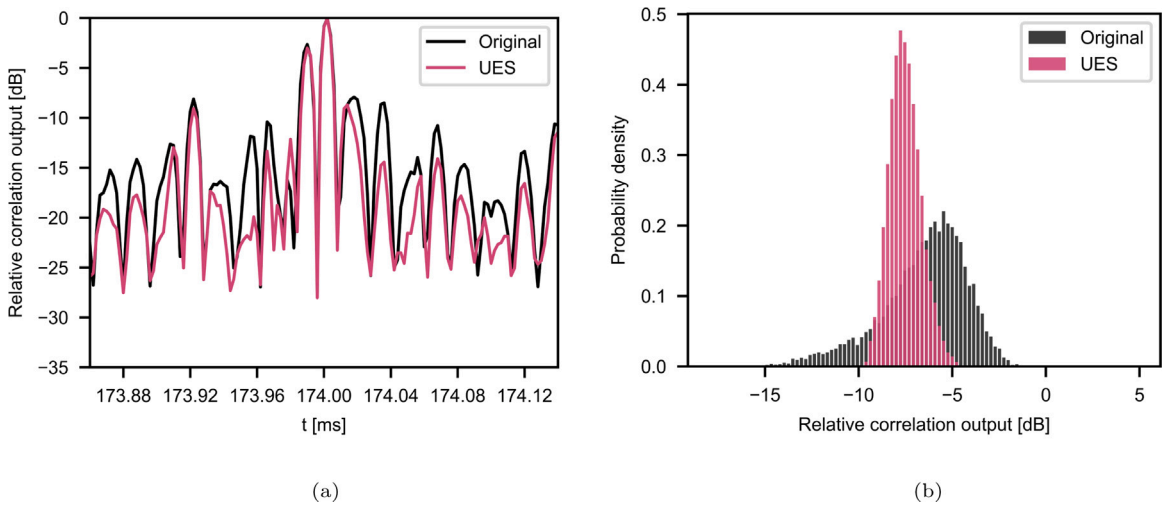

Fig. 11. Self and mutual interference in setup 2. (a) Averaged self-interference zoomed to the correlation peak area. (b) Histogram of the maximum dB modulus of all mutual interferences.

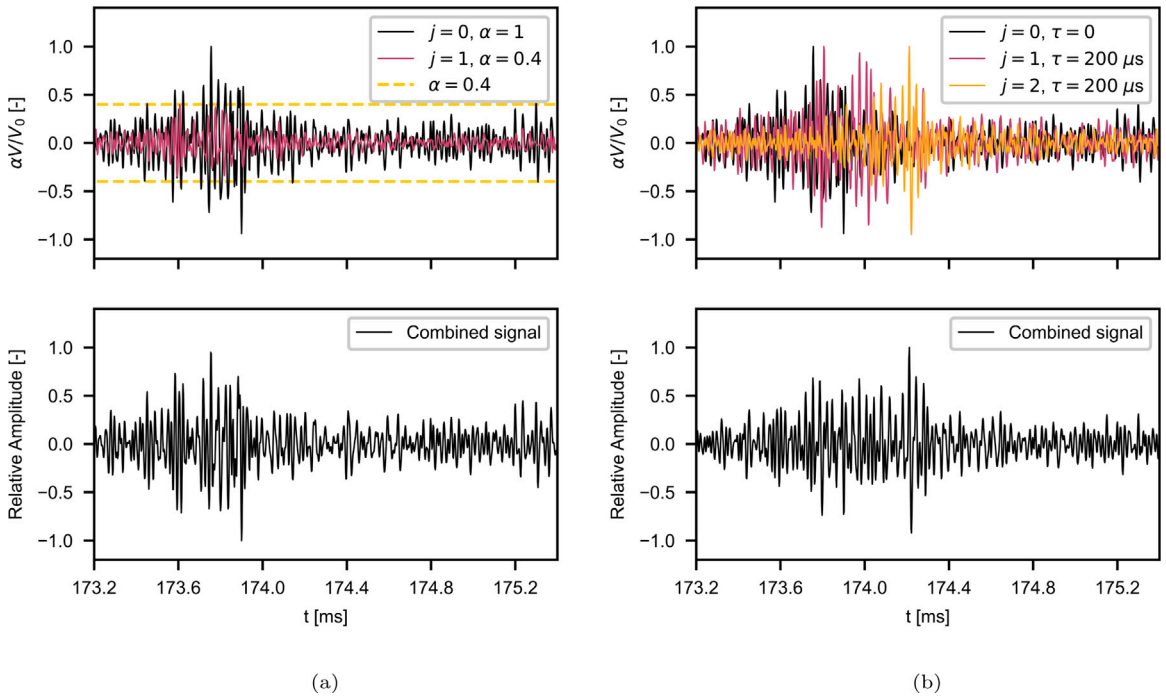

Fig. 12. Examples of the construction of semi-synthetic MIMO signals. (a) Two signals with different scaling factors α (top) and the corresponding combined signal (bottom). (b) Three signals with time shift $j\tau$ (top) and the corresponding combined signal (bottom).

it more difficult to visually identify the first pulse in the combined signal. To find the TOF of the first arriving pulse, the combined signal is correlated with the microphone reference signal of the first pulse so that $\tilde{R}_{st} = \tilde{s}_r(t) * s_{t,0}$. To validate that the TOF was found correctly, the correlation maximum of $\tilde{R}_{st}$ was compared with the maximum of the respective unmodified signal pair $R_{st,0} = s_{r,0} * s_{t,0}$. To exclude dependence of consecutive pulses, 1000 combinations of $s_{r,j}$ were pseudo-randomly sampled. To assess the applicability of fluidic transducer signals in MIMO setups, the true-false ratio of the correlation maxima as well as the mean TOF error associated with the erroneous maxima were compared.

Figs. 13 and 14 show the results of the synthetic MIMO experiments. The TOF estimation error is highly dependent on the time shift between the combined signals. For both the original and the envelope-extracted signals, the number of incorrectly estimated signals was highest at small time shifts. When $\tilde{s}_r(t)$ contains two signals, the true-false ratio reaches a minimum of 0.65 for the unmodified signal and 0.83 for the UES (Fig. 13(a)). For $\tilde{s}_r(t)$ containing four signals, these fractions decreased to 0.4 and 0.55, respectively (Fig. 14(a)). The fractions increased with the delay of the successive signals and reached a plateau at time shifts larger than 1–1.5 ms with values above 0.9, which approximately represents the duration of the pulse, shown in Fig. 3. At these large time shifts, the pulse signals superimposed with largely lower amplitudes and different frequency contents, so that there was little mutual interference. For all time shifts, the true-false ratio decreased further when the successive pulses were attenuated, reducing their influence in terms of both spectral signature and amplitude. The TOF error of the misidentified pulses showed a similar trend. In general, the absolute errors were higher in the small-shift region, where there was larger mutual interference between the pulses. For two successive pulses (Fig. 13(b)), the mean TOF error was below 12 µs for the unmodified signal and below 6 µs for the UES for all time shifts investigated, except

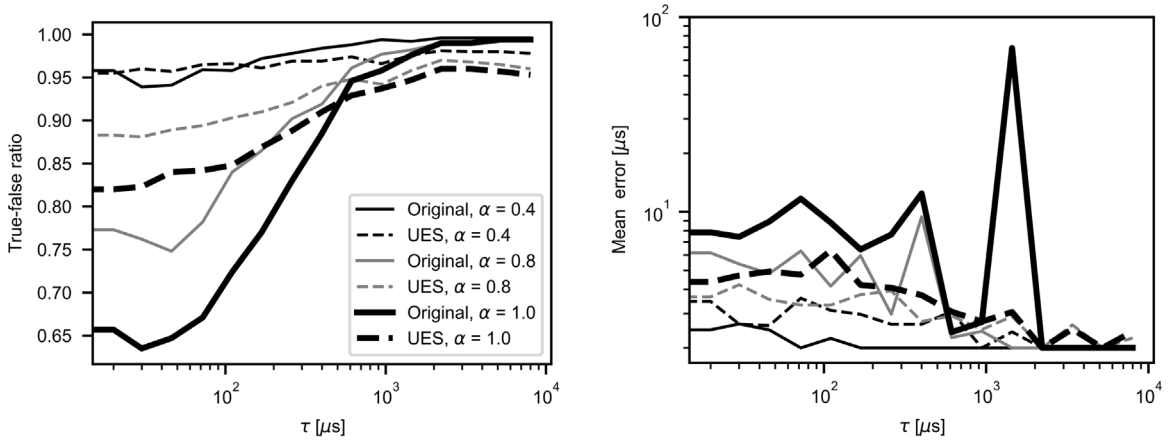

Fig. 13. (a) Accuracy for the semi-synthetic experiment using 2 subsequent pulses and (b) mean error of inaccurately identified TOFs.

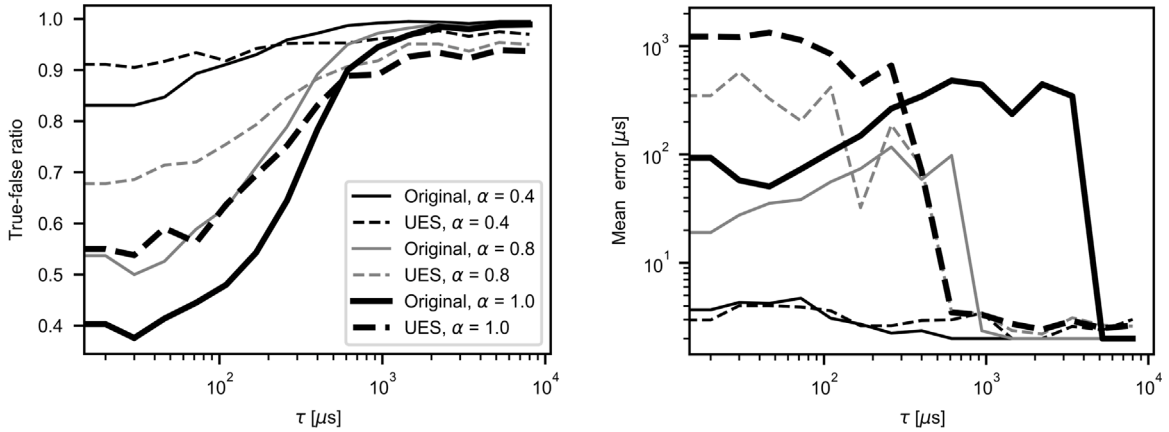

Fig. 14. (a) Accuracy for the semi-synthetic experiment using 4 subsequent pulses and (b) mean error of inaccurately identified TOFs.

for one outlier. The cause of the spike of the unattenuated original signal at a shift of 1.44 ms is unclear. As the signal is attenuated, the mean error reduced. Furthermore, the advantage of correlating the UES decreased for $\alpha = 0.8$ and reversed for $\alpha = 0.4$ at low level. When a received train of four pulses was synthesized (Fig. 14(b)), the TOF error of the unmodified signal increased with time shift up to 400 μs as the following pulses gave higher correlation results than the first, until a sharp drop at high shifts. When UES was used for correlation, the TOF error increased even further by an order of magnitude before dropping to single digits. Even considering the higher true-false ratio, envelope extraction results in a less accurate TOF estimate in the four-pulse MIMO setup. Thus the choice of the number of transmitters and receivers in a MIMO setup is highly dependent on the noise situation in the application and the required accuracy. If the received pulses are expected to have similar amplitudes and arrival times, only a few number of transducers should be used. In case multiple receivers are placed at a sufficient distance so that the pulse amplitude and TOF differ largely, more transmitters may be used. In all cases, removing the envelope causes an increased true-false ratio for small TOF shifts, compared to the original signal.

5. Conclusions

In this study, the mutual and self-interference characteristics of the novel fluidic transducer and its suitability for MIMO applications were investigated. To this end, the fluidic transducer signal was interpreted as a random amplitude and angle-modulated signal.

Using only the acoustic signal in air, the signal envelope has a significant influence on the mutual interference of the pulses. Removing the amplitude information using Hilbert envelope extraction leaves only the pulses' spectral signature with a unit envelope. The remaining angle modulated pulses are quasi-orthogonal. The mean mutual correlation maximum was reduced by 3 dB and its standard deviation by 1.4 dB, indicating a significant increase in the discriminability between pulses. Furthermore, the self-interference close to the correlation maximum was slightly reduced. However, removing the envelope information resulted in a noise floor increase from −40 dB to −30 dB outside the peak range of the fluidic transducer signal.

This behavior was confirmed in a second setup. The signal was transmitted through a thin aluminum sheet, the reference pulse was measured with a microphone whereas, while the received signal was recorded with an accelerometer. Significantly less mutual interference was found. However, the advantages of envelope removal were lessened when noise was present in the received signal. Using the same measurement data, semi-synthetic experiments were realized to simulate receiving multiple pulses by the accelerometer in a MIMO setup. For pulses arriving in close succession, the unit envelope signals consistently had a higher detection rate of the correct correlation maximum. The results also showed the sensitivity of the UES correlation to channel

noise, resulting in larger average TOF estimation errors as the number of received pulses was increased. Thus, depending on the application, the fluidic transducer is suitable for MIMO applications when the SNR is high, the number of transmitter–receiver pairs is low, or they are far enough apart to reduce interference amplitude.

The advanced signal processing presented here increases the signal-to-noise ratio by an additional 3 dB. Furthermore, the fluidic devices are very robust, require only pressurized air, are maintenance-free and thus highly applicable even in harsh environments. These new transducers in combination with the optimized TOF computation make it a very promising method for air-coupled ultrasound in NDT. Future research will investigate the applicability of the fluidic transducer and the here presented demodulation method to various NDT tasks.

CRediT authorship contribution statement

Benjamin Bühling: Conceptualization, Methodology, Investigation, Validation, Formal analysis, Visualization, Writing – original draft, Software, Data curation. **Stefan Maack:** Supervision, Project administration, Writing – review & editing, Funding acquisition. **Thorge Schweitzer:** Resources, Writing – review & editing. **Christoph Strangfeld:** Supervision, Project administration, Writing – review & editing, Funding acquisition.

Declaration of competing interest

One or more of the authors of this paper have disclosed potential or pertinent conflicts of interest, which may include receipt of payment, either direct or indirect, institutional support, or association with an entity in the biomedical field which may be perceived to have potential conflict of interest with this work. For full disclosure statements refer to https://doi.org/10.1016/j.ultras.2021.106612. The Federal Institute for Materials Research and Testing (BAM), the employer of B. Bühling, C. Strangfeld, S. Maack, is holding a patent concerning air-coupled ultrasound generation using fluidic oscillators [32] of which C. Strangfeld and S. Maack are the inventors. T. Schweitzer is employed by FDX Fluid Dynamix GmbH, a company that develops and sells fluidic-based products.

Acknowledgments

The authors would like to thank Mate Gaal (BAM 8.4) for support with the acoustic measurements and Christian Köpp (BAM 8.2) for his helpful feedback.

Funding

This work was supported by the Federal Ministry for Economic Affairs and Energy (BMWi) under the ZIM (Zentrales Innovationsprogramm Mittelstand) Grant No. ZF4044222WM7.

References

[1] T.L. Szabo, Diagnostic Ultrasound Imaging, Vol. 1, Academic Press, Burlington, 2004, http://dx.doi.org/10.1016/B978-012680145-3/50015-3.

[2] T. Verellen, R. Kerstens, J. Steckel, High-resolution ultrasound sensing for robotics using dense microphone arrays, IEEE Access 8 (2020) 190083–190093, http://dx.doi.org/10.1109/ACCESS.2020.3032177.

[3] J. Krautkrämer, H. Krautkrämer, Ultrasonic Testing of Materials, fourth ed., Springer Berlin Heidelberg, Berlin, Heidelberg, 1990, http://dx.doi.org/10.1007/978-3-662-10680-8.

[4] J. Krautkrämer, H. Krautkrämer, The shadow method, in: J. Krautkrämer, H. Krautkrämer (Eds.), Ultrasonic Testing of Materials, Springer Berlin Heidelberg, Berlin, Heidelberg, 1990, pp. 239–240, http://dx.doi.org/10.1007/978-3-662-10680-8_13.

[5] Y. Fang, L. Lin, H. Feng, Z. Lu, G.W. Emms, Review of the use of air-coupled ultrasonic technologies for nondestructive testing of wood and wood products, Comput. Electron. Agric. 137 (2017) 79–87, http://dx.doi.org/10.1016/j.compag.2017.03.015.

[6] M.V. Felice, Z. Fan, Sizing of flaws using ultrasonic bulk wave testing: A review, Ultrasonics 88 (2018) 26–42, http://dx.doi.org/10.1016/j.ultras.2018.03.003.

[7] B.S. Marció, A.A. Seibert, G.d.A. Braz, A.A.O. Carneiro, R.C.C. Flesch, Nondestructive inspection of metal specimen using tone-burst vibro-acoustography, Ultrasonics 111 (2021) 106339, http://dx.doi.org/10.1016/j.ultras.2020.106339.

[8] S.D. Holland, D.E. Chimenti, High contrast air-coupled acoustic imaging with zero group velocity lamb modes, Ultrasonics 42 (1) (2004) 957–960, http://dx.doi.org/10.1016/j.ultras.2003.12.009.

[9] T.E. Gómez Álvarez-Arenas, A nondestructive integrity test for membrane filters based on air-coupled ultrasonic spectroscopy, IEEE Trans. Ultrason. Ferroelectr. Freq. Control 50 (6) (2003) 676–685, http://dx.doi.org/10.1109/TUFFC.2003.1209555.

[10] T.E. Gómez Álvarez-Arenas, J. Camacho, Air-coupled and resonant pulse-echo ultrasonic technique, Sensors 19 (10) (2019) http://dx.doi.org/10.3390/s19102221.

[11] T.P. Lerch, Ultrasonic thickness measurement of nonporous membranes with long wavelengths, Ultrasonics 113 (2021) 106370, http://dx.doi.org/10.1016/j.ultras.2021.106370.

[12] T.P. Philippidis, D.G. Aggelis, Experimental study of wave dispersion and attenuation in concrete, Ultrasonics 43 (7) (2005) 584–595, http://dx.doi.org/10.1016/j.ultras.2004.12.001.

[13] J. Gosálbez, W.M.D. Wright, W. Jiang, A. Carrión, V. Genovés, I. Bosch, Airborne non-contact and contact broadband ultrasounds for frequency attenuation profile estimation of cementitious materials, Ultrasonics 88 (2018) 148–156, http://dx.doi.org/10.1016/j.ultras.2018.03.011.

[14] E.N. Landis, E. Hassefras, T.S. Oesch, E. Niederleithinger, Relating ultrasonic signals to concrete microstructure using X-ray computed tomography, Constr. Build. Mater. 268 (2021) 121124, http://dx.doi.org/10.1016/j.conbuildmat.2020.121124.

[15] T.E. Gómez Álvarez-Arenas, M.D. Fariñas, A. Ginel, Fast and non-destructive ultrasonic test for face masks, Ultrasonics 117 (2021) 106556, http://dx.doi.org/10.1016/j.ultras.2021.106556.

[16] D.K. Hsu, Non-destructive evaluation (NDE) of aerospace composites: ultrasonic techniques, in: V.M. Karbhari (Ed.), Non-Destructive Evaluation (NDE) of Polymer Matrix Composites, Woodhead Publishing, 2013, pp. 397–422, http://dx.doi.org/10.1533/9780857093554.3.397.

[17] J. Rus, A. Gustschin, H. Mooshofer, J.-C. Grager, K. Bente, M. Gaal, F. Pfeiffer, C.U. Grosse, Qualitative comparison of non-destructive methods for inspection of carbon fiber-reinforced polymer laminates, J. Compos. Mater. 54 (27) (2020) 4325–4337, http://dx.doi.org/10.1177/0021998320931162.

[18] S. Maack, S. Küttenbaum, N. Epple, M. Aligholizadeh, Die Ultraschall-Echomethode – von der Messung zur bautechnischen Kenngröße [Ultrasonic Echo Method – Deriving structural parameters from measured values], Beton- Stahlbetonbau 116 (3) (2021) 200–211, http://dx.doi.org/10.1002/best.202000091.

[19] V. Dayal, An automated simultaneous measurement of thickness and wave velocity by ultrasound, Exp. Mech. 32 (3) (1992) 197–202, http://dx.doi.org/10.1007/BF02319355.

[20] T.E. Gómez Álvarez-Arenas, Simultaneous determination of the ultrasound velocity and the thickness of solid plates from the analysis of thickness resonances using air-coupled ultrasound, Ultrasonics 50 (2) (2010) 104–109, http://dx.doi.org/10.1016/j.ultras.2009.09.009.

[21] K. Tsuji, T. Norisuye, H. Nakanishi, Q. Tran-Cong-Miyata, Simultaneous measurements of ultrasound attenuation, phase velocity, thickness, and density spectra of polymeric sheets, Ultrasonics 99 (2019) 105974, http://dx.doi.org/10.1016/j.ultras.2019.105974.

[22] J. Krautkrämer, H. Krautkrämer, Attenuation of ultrasonic waves in solids, in: J. Krautkrämer, H. Krautkrämer (Eds.), Ultrasonic Testing of Materials, Springer Berlin Heidelberg, Berlin, Heidelberg, 1990, pp. 108–116, http://dx.doi.org/10.1007/978-3-662-10680-8_7.

[23] T.H. Gan, D.A. Hutchins, D.R. Billson, D.W. Schindel, The use of broadband acoustic transducers and pulse-compression techniques for air-coupled ultrasonic imaging, Ultrasonics 39 (3) (2001) 181–194, http://dx.doi.org/10.1016/S0041-624X(00)00059-7.

[24] H. Tat, G. Georgeson, R. Bossi, Evaluation of air coupled ultrasound for composite aerospace structure, AIP Conf. Proc. 1096 (1) (2009) 912–919, http://dx.doi.org/10.1063/1.3114355.

[25] R.G. Maev, R.E. Green, A.M. Siddiolo, Review of advanced acoustical imaging techniques for nondestructive evaluation of art objects, Res. Nondestruct. Eval. 17 (4) (2006) 191–204, http://dx.doi.org/10.1080/09349840600981088.

[26] D.E. Chimenti, Review of air-coupled ultrasonic materials characterization, Ultrasonics 54 (7) (2014) 1804–1816, http://dx.doi.org/10.1016/j.ultras.2014.02.006.

[27] B. Gräfe, Luftgekoppeltes Ultraschallecho-Verfahren für Betonbauteile [Air-coupled ultrasonic echo method for concrete structures] (Ph.D. thesis), 2009, http://dx.doi.org/10.14279/depositonce-1964.

[28] R.J. Kazys, R. Sliteris, J. Sestoke, Air-coupled low frequency ultrasonic transducers and arrays with PMN-32%PT piezoelectric crystals, Sensors 17 (1) (2017) http://dx.doi.org/10.3390/s17010095.

[29] X. Wang, X. Gong, C. Li, R. Wu, Z. Chen, H. Wu, D. Zhang, X. Cao, Low insertion loss air-coupled ultrasonic transducer with parallel laminated piezoelectric structure, AIP Adv. 10 (10) (2020) 105331, http://dx.doi.org/10.1063/5.0022598.

[30] S.T. Hansen, B.J. Mossawir, A.S. Ergun, F.L. Degertekin, B.T. Khuri-Yakub, Air-coupled nondestructive evaluation using micromachined ultrasonic transducers, in: IEEE Ultrasonics Symp., Vol. 2, 1999, pp. 1037–1040, http://dx.doi.org/10.1109/ULTSYM.1999.849177.

[31] S.P. Kelly, G. Hayward, T.E. Gómez Álvarez-Arenas, Characterization and assessment of an integrated matching layer for air-coupled ultrasonic applications, IEEE Trans. Ultrason. Ferroelectr. Freq. Control 51 (10) (2004) 1314–1323, http://dx.doi.org/10.1109/TUFFC.2004.1350960.

[32] V.T. Rathod, A review of acoustic impedance matching techniques for piezoelectric sensors and transducers, Sensors 20 (14) (2020) http://dx.doi.org/10.3390/s20144051.

[33] R. Kressmann, New piezoelectric polymer for air-borne and water-borne sound transducers, J. Acoust. Soc. Am. 109 (4) (2001) 1412–1416, http://dx.doi.org/10.1121/1.1354989.

[34] T.E. Gómez Álvarez-Arenas, Air-coupled piezoelectric transducers with active polypropylene foam matching layers, Sensors 13 (5) (2013) http://dx.doi.org/10.3390/s130505996.

[35] M. Gaal, D. Kotschate, K. Bente, Advances in air-coupled ultrasonic transducers for non-destructive testing, Proc. Meet. Acoust. 38 (1) (2019) 1–7, http://dx.doi.org/10.1121/2.0001072.

[36] D.A. Hutchins, Ultrasonic generation by pulsed lasers, in: W.P. Mason, R.N. Thurston (Eds.), Physical Acoustics, Vol. 18, Academic Press, San Diego, 1988, pp. 21–123, http://dx.doi.org/10.1016/B978-0-12-477918-1.50008-4.

[37] S.-C. Hong, A.-D. Abetew, J.-R. Lee, J.-B. Ihn, Three dimensional evaluation of aluminum plates with wall-thinning by full-field pulse-echo laser ultrasound, Opt. Lasers Eng. 99 (2017) 58–65, http://dx.doi.org/10.1016/j.optlaseng.2016.08.010.

[38] K.Y. Kim, W. Sachse, X-ray generated ultrasound, Appl. Phys. Lett. 43 (12) (1983) 1099–1101, http://dx.doi.org/10.1063/1.94240.

[39] S. Tang, C. Ramseyer, P. Samant, L. Xiang, X-ray-induced acoustic computed tomography of concrete infrastructure, Appl. Phys. Lett. 112 (6) (2018) 1–5, http://dx.doi.org/10.1063/1.5009936.

[40] T. Tran, P. Samant, L. Xiang, Y. Liu, X-Ray induced acoustic computed tomography for non-destructive testing of aircraft structure, in: Proc. IMECE2019, Vol. 1, ASME, 2019, pp. 1–5, http://dx.doi.org/10.1115/IMECE2019-10480.

[41] B. Hosten, P.A. Bernard, Ultrasonic wave generation by time-gated microwaves, J. Acoust. Soc. Am. 104 (2) (1998) 860–866, http://dx.doi.org/10.1121/1.423309.

[42] E. Guilliorit, B. Hosten, C. Bacon, D.E. Chimenti, Microwave excitation of ultrasound in graphite–fiber reinforced composite plates, Ultrasonics 41 (2) (2003) 97–103, http://dx.doi.org/10.1016/S0041-624X(02)00432-8.

[43] H. Shinoda, T. Nakajima, K. Ueno, N. Koshida, Thermally induced ultrasonic emission from porous silicon, Nature 400 (6747) (1999) 853–855, http://dx.doi.org/10.1038/23664.

[44] M. Daschewski, R. Boehm, J. Prager, M. Kreutzbruck, A. Harrer, Physics of thermo-acoustic sound generation, J. Appl. Phys. 114 (11) (2013) 1–12, http://dx.doi.org/10.1063/1.4821121.

[45] J. Song, Y. Li, Y. Li, G. Liu, Three-dimensional model of thermoacoustic tomography with electric excitation, J. Appl. Phys. 124 (16) (2018) 164902, http://dx.doi.org/10.1063/1.5045510.

[46] D. Kotschate, M. Gaal, H. Kersten, Acoustic emission by self-organising effects of micro-hollow cathode discharges, Appl. Phys. Lett. 112 (15) (2018) 1–4, http://dx.doi.org/10.1063/1.5024459.

[47] D. Kotschate, S. Wendland, M. Gaal, Airborne testing of molded polymer compounds, in: 10th International Symposium on NDT in Aerospace (Proceedings), Vol. 168, 2018, pp. 1–7, Th.6.C.1, URL https://opus4.kobv.de/opus4-bam/frontdoor/index/index/docId/46560.

[48] B. Bühling, C. Strangfeld, S. Maack, T. Schweitzer, Experimental analysis of the acoustic field of an ultrasonic pulse induced by a fluidic switch, J. Acoust. Soc. Am. 149 (4) (2021) 2150–2158, http://dx.doi.org/10.1121/10.0003937.

[49] T. Schweitzer, M. Hörmann, B. Bühling, B. Bobusch, Switching action of a bistable fluidic amplifier for ultrasonic testing, Fluids 6 (5) (2021) 171, http://dx.doi.org/10.3390/fluids6050171.

[50] R.W. Warren, Some parameters affecting the design of bistable fluid amplifiers, in: F.T. Brown (Ed.), Fluid Jet Control Devices: Papers Presented At the Winter Annual Meeting of the ASME, American Society of Mechanical Engineers, New York, 1962, pp. 75–82, URL https://books.google.de/books/about/Symposium_on_Fluid_Jet_Control_Devices_a.html?id=b1BdjwEACAAJ&redir_esc=y.

[51] B.C. Bobusch, Fluidic Devices for Realizing the Shockless Explosion Combustion Process (Ph.D. thesis), 2015, http://dx.doi.org/10.14279/depositonce-4351.

[52] S.L. McBride, T.S. Hutchison, Helium gas jet spectral calibration of acoustic emission transducers and systems, Can. J. Phys. 54 (17) (1976) 1824–1830, http://dx.doi.org/10.1139/p76-216.

[53] D.W. Choi, C. McIntyre, D.A. Hutchins, D.R. Billson, Gas jet as a waveguide for air-coupled ultrasound, Ultrasonics 40 (1) (2002) 145–151, http://dx.doi.org/10.1016/S0041-624X(02)00128-2.

[54] V.L. Newhouse, E.S. Furgason, N.M. Bilgutay, G.R. Cooper, Random signal flaw detection, in: IEEE Ultrasonics Symp., 1974, pp. 712–715, http://dx.doi.org/10.1109/ULTSYM.1974.196431.

[55] E.S. Furgason, V.L. Newhouse, N.M. Bilgutay, G.R. Cooper, Application of random signal correlation techniques to ultrasonic flaw detection, Ultrasonics 13 (1) (1975) 11–17, http://dx.doi.org/10.1016/0041-624X(75)90017-7.

[56] N.M. Bilgutay, E.S. Furgason, V.L. Newhouse, Evaluation of a random signal correlation system for ultrasonic flaw detection, IEEE Trans. Sonics. Ultrason. 23 (5) (1976) 329–333, http://dx.doi.org/10.1109/T-SU.1976.30886.

[57] C.M. Elias, An ultrasonic pseudorandom signal-correlation system, IEEE Trans. Sonics. Ultrason. 27 (1) (1980) 1–6, http://dx.doi.org/10.1109/T-SU.1980.31136.

[58] B.B. Lee, E.S. Furgason, High-speed digital golay code flaw detection system, Ultrasonics 21 (4) (1983) 153–161, http://dx.doi.org/10.1016/0041-624X(83)90070-7.

[59] J.Y. Chapelon, Pseudo-random correlation imaging and system characterization, in: V.L. Newhouse (Ed.), Progress in Medical Imaging, Springer New York, New York, NY, 1988, pp. 227–246, http://dx.doi.org/10.1007/978-1-4612-3866-9_6.

[60] S.W. Golomb, G. Gong, Signal Design for Good Correlation: For Wireless Communication, Cryptography, and Radar, Cambridge University Press, Cambridge, 2005, http://dx.doi.org/10.1017/CBO9780511546907.

[61] S. Caporale, S. Callegari, M. Ricci, P. Burrascano, Constant envelope pseudo orthogonal excitations for ultrasound testing, in: 18th Int. Conf. Digit. Signal Process., 2013, pp. 1–8, http://dx.doi.org/10.1109/ICDSP.2013.6622751.

[62] C. Leavens, R. Willams, P. Burns, M. Sherar, The use of phase codes in ultrasound imaging: SNR gain and bandwidth requirements, Appl. Acoust. 70 (10) (2009) 1340–1351, http://dx.doi.org/10.1016/j.apacoust.2008.10.005.

[63] L. Svilainis, A. Aleksandrovas, Application of arbitrary pulse width and position trains for the correlation sidelobes reduction for narrowband transducers, Ultrasonics 53 (7) (2013) 1344–1348, http://dx.doi.org/10.1016/j.ultras.2013.04.001.

[64] M. Ricci, S. Callegari, S. Caporale, M. Monticelli, L. Battaglini, M. Eroli, L. Senni, R. Rovatti, G. Setti, P. Burrascano, Exploiting non-linear chirp and sparse deconvolution to enhance the performance of pulse-compression ultrasonic NDT, in: IEEE Intern. Ultrasonics Symp., 2012, pp. 1489–1492, http://dx.doi.org/10.1109/ULTSYM.2012.0372.

[65] M. Ricci, L. Senni, P. Burrascano, R. Borgna, S. Neri, M. Calderini, Pulse-compression ultrasonic technique for the inspection of forged steel with high attenuation, Insight, Non-Destr. Test. Cond. Monit. 54 (2) (2012) 91–95, http://dx.doi.org/10.1784/insi.2012.54.2.91.

[66] D.A. Hutchins, R.L. Watson, L.A.J. Davis, L. Akanji, D.R. Billson, P. Burrascano, S. Laureti, M. Ricci, Ultrasonic propagation in highly attenuating insulation materials, Sensors 20 (8) (2020) http://dx.doi.org/10.3390/s20082285.

[67] D. Hutchins, P. Burrascano, L. Davis, S. Laureti, M. Ricci, Coded waveforms for optimised air-coupled ultrasonic nondestructive evaluation, Ultrasonics 54 (7) (2014) 1745–1759, http://dx.doi.org/10.1016/j.ultras.2014.03.007.

[68] S. Callegari, M. Ricci, S. Caporale, M. Monticelli, M. Eroli, L. Senni, R. Rovatti, G. Setti, P. Burrascano, From chirps to random-FM excitations in pulse compression ultrasound systems, in: IEEE Intern. Ultrasonics Symp., 2012, pp. 471–474, http://dx.doi.org/10.1109/ULTSYM.2012.0117.

[69] A.D. Pierce, Low-frequency models of sound transmission, in: A.D. Pierce (Ed.), Acoustics: An Introduction to Its Physical Principles and Applications, Springer International Publishing, Cham, 2019, pp. 361–426, http://dx.doi.org/10.1007/978-3-030-11214-1_7.

[70] K.S. Hall, Air-coupled Ultrasonic Tomographic Imaging of Concrete Elements (Ph.D. thesis), 2011, URL http://hdl.handle.net/2142/26142.

[71] A.D. Pierce, Radiation from vibrating bodies, in: A.D. Pierce (Ed.), Acoustics: An Introduction to Its Physical Principles and Applications, Springer International Publishing, Cham, 2019, pp. 177–239, http://dx.doi.org/10.1007/978-3-030-11214-1_4.

[72] X. Dai, J. Zhu, M.R. Haberman, A focused electric spark source for non-contact stress wave excitation in solids, J. Acoust. Soc. Am. 134 (6) (2013) EL513–EL519, http://dx.doi.org/10.1121/1.4826913.

[73] H. Jain, V.H. Patankar, Embedded system for ultrasonic imaging of under-water concrete structures, J. Instrum. 16 (07) (2021) P07049, http://dx.doi.org/10.1088/1748-0221/16/07/p07049.

[74] K.J. Vössing, E. Niederleithinger, Nondestructive assessment and imaging methods for internal inspection of timber. A review, Holzforschung 72 (6) (2018) 467–476, http://dx.doi.org/10.1515/hf-2017-0122.

[75] Y. Shmaliy, Signals modulation, in: Y. Shmaliy (Ed.), Continuous-Time Signals, Springer Netherlands, Dordrecht, 2006, pp. 131–200, http://dx.doi.org/10.1007/978-1-4020-4818-0_3.

[76] I.J. Moon, S.H. Hong, What is temporal fine structure and why is it important? Korean J. Audiol. 18 (1) (2014) 1–7, http://dx.doi.org/10.7874/kja.2014.18.1.1.

[77] B. Boashash, Estimating and interpreting the instantaneous frequency of a signal. I. Fundamentals, Proc. IEEE 80 (4) (1992) 520–538, http://dx.doi.org/10.1109/5.135376.

[78] L. Cohen, C. Lee, Instantaneous frequency, its standard deviation and multicomponent signals, Proc. SPIE 0975 (1988) http://dx.doi.org/10.1117/12.948504.

[79] B.J. Rickett, Amplitude-modulated noise: an empirical model for the radio radiation received from pulsars, Astrophys. J. 197 (1975) 185–191, http://dx.doi.org/10.1086/153501.

[80] O. Ponomareva, A. Ponomarev, N. Smirnova, Hilbert envelope extraction from real discrete finite signals considering the nonlocality of Hilbert transform, in: 2020 22th Int. Conf. Digit. Signal Process. Appl., 2020, pp. 1–4, http://dx.doi.org/10.1109/DSPA48919.2020.9213286.

[81] P.Y. Ktonas, N. Papp, Instantaneous envelope and phase extraction from real signals: Theory, implementation, and an application to EEG analysis, Signal Process. 2 (4) (1980) 373–385, http://dx.doi.org/10.1016/0165-1684(80)90079-1.

[82] N. Delprat, B. Escudie, P. Guillemain, R. Kronland-Martinet, P. Tchamitchian, B. Torresani, Asymptotic wavelet and gabor analysis: extraction of instantaneous frequencies, IEEE Trans. Inform. Theory 38 (2) (1992) 644–664, http://dx.doi.org/10.1109/18.119728.

[83] B. Picinbono, On instantaneous amplitude and phase of signals, IEEE Trans. Signal Process. 45 (3) (1997) 552–560, http://dx.doi.org/10.1109/78.558469.

[84] L.V. Vela-Arevalo, Time-frequency Analysis Based on Wavelets for Hamiltonian Systems (Ph.D. thesis), 2002, http://dx.doi.org/10.7907/8MBB-3Z60.

[85] M. Feldman, A signal decomposition or lowpass filtering with Hilbert transform? Mech. Syst. Signal Process. 25 (8) (2011) 3205–3208, http://dx.doi.org/10.1016/j.ymssp.2011.04.016.

[86] O. Ghitza, On the upper cutoff frequency of the auditory critical-band envelope detectors in the context of speech perception, J. Acoust. Soc. Am. 110 (3) (2001) 1628–1640, http://dx.doi.org/10.1121/1.1396325.

[87] S. Schimmel, L. Atlas, Coherent envelope detection for modulation filtering of speech, in: Proc. - ICASSP IEEE Int. Conf. Acoust. Speech Signal Process, Vol. 1, 2005, pp. I/221–I/224, http://dx.doi.org/10.1109/ICASSP.2005.1415090.